nature materials

SUPPLEMENTARY INFORMATION

DOI: 10.1038/NMAT4430

Convergence of multi-valley bands as the electronic origin of high thermoelectric performance in $CoSb_3$ skutterudites

Yinglu Tang[ab], Zachary M. Gibbs*[c], Luis A. Agapito[de], Guodong Li[abf], Hyun-Sik Kim[abg], Marco Buongiorno Nardelli[d], Stefano Curtarolo[e], G. Jeffrey Snyder[ab]*

*Contributed equally to this work

[a] Department of Materials Science and Engineering, Northwestern University, Evanston, Illinois 60208, USA
Correspondence and requests for materials should be addressed to G. Jeffrey Snyder (E-mail: jeff.snyder@northwestern.edu)

[b] Department of Applied Physics and Materials Science, California Institute of Technology, Pasadena, California 91125, USA

[c] Division of Chemistry and Chemical Engineering, California Institute of Technology, Pasadena, California 91125, USA

[d] Department of Physics, University of North Texas, Denton, Texas 76203, USA

[e] Department of Materials Science and Physics, Duke University, Durham, North Carolina 27708, USA

[f] School of Science, Wuhan University of Technology, Wuhan, Hubei 430070, China

[g] Materials Research Center, Samsung Advanced Institute of Technology, Samsung Electronics, Suwon 443-803, South Korea

DOI: 10.1038/NMAT4430

Structural Characterization

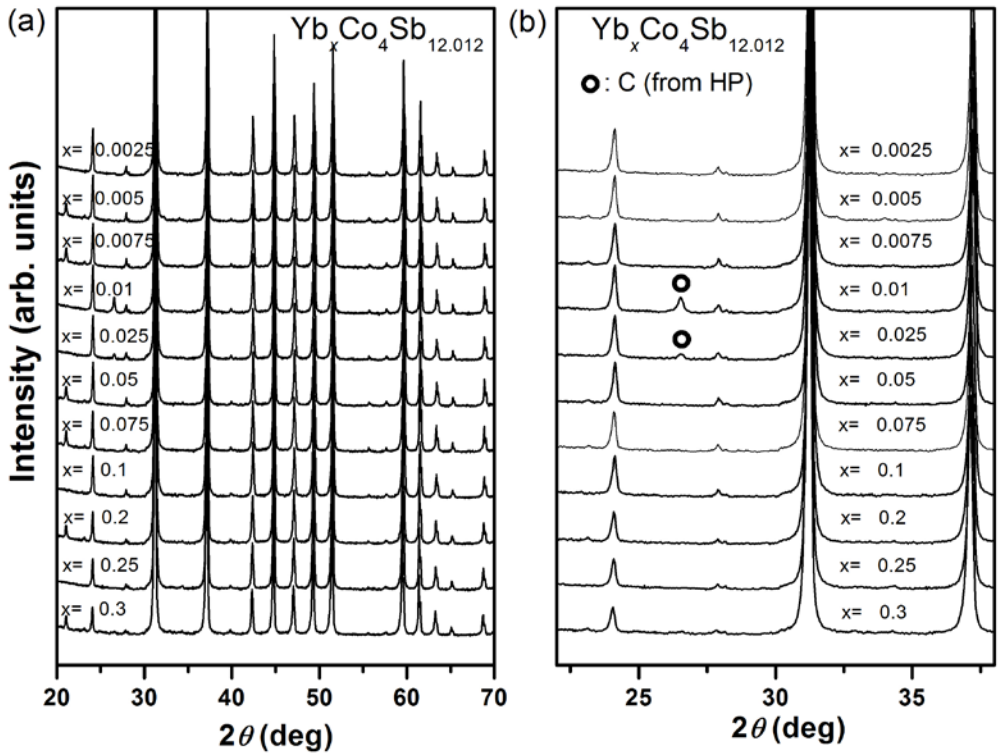

Figure S1. (a) XRD patterns of the Yb-doped skutterudite pellets after hot press (HP) with nominal compositions $Yb_xCo_4Sb_{12.012}$ (x ranging from 0.0025 to 0.3). (b) Magnification of the XRD patterns in (a).

Figure S1 (a, b) shows the X-ray diffraction results of Yb-doped skutterudites annealed and hot pressed at 973K with nominal compositions $Yb_xCo_4Sb_{12.012}$ (x ranging from 0.0025 to 0.3). All major diffraction peaks are indexable to the skutterudite phase, as identified using Powder Diffraction File reference number 01-078-0976 for $CoSb_3$ in International Center for Diffraction Data (ICDD). For x=0.01 and x=0.025 samples, a carbon peak was detected at around 26.6°, which is from the residual carbon coating during hot press.

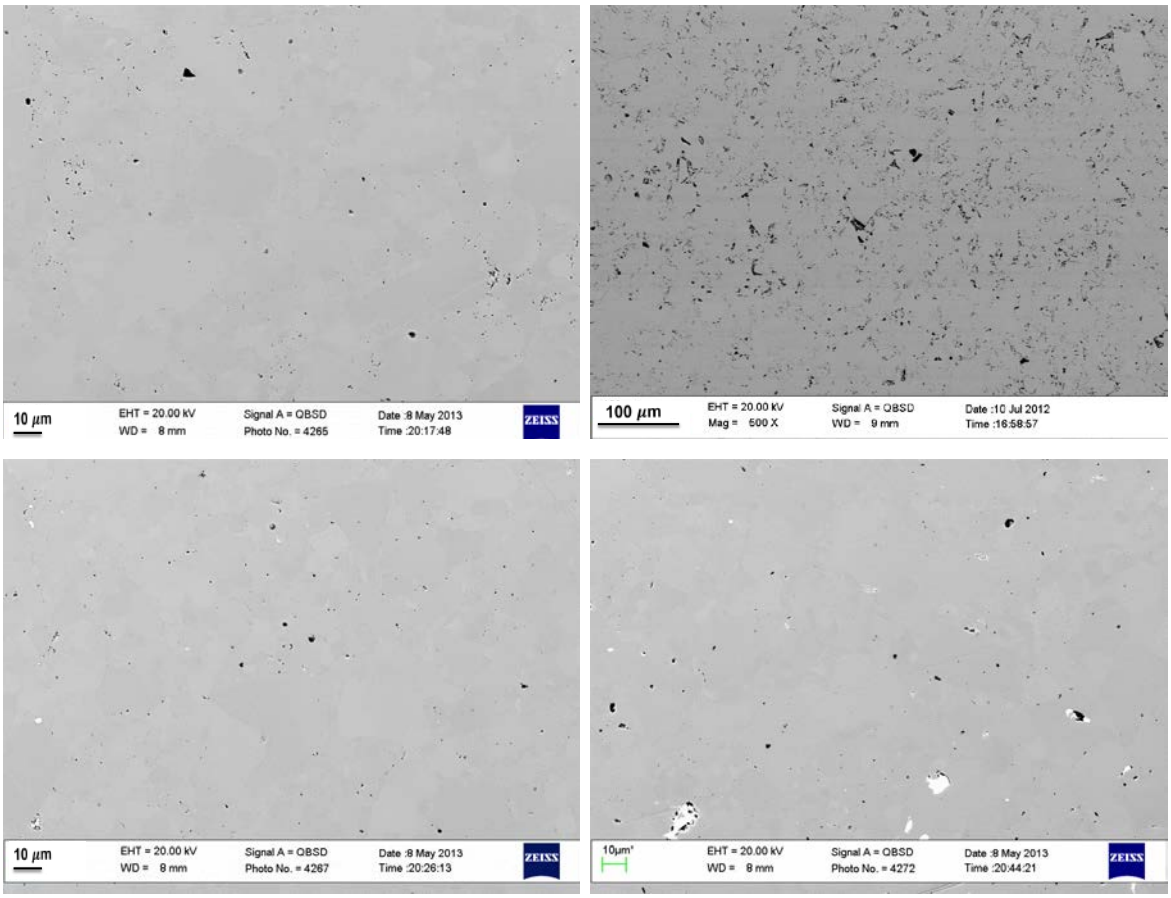

Figure S2. Scanning electron microscope (SEM) images of hot pressed samples with (a) $x = 0.10$; (b) $x = 0.20$; (c) $x = 0.25$; (d) $x = 0.30$. The black regions are holes formed by thermal contraction during quenching. The white phase on (c, d) is Yb-rich impurities, which may form due to sample inhomogeneity.

Scanning electron microscope (SEM) images were taken for all 11 samples annealed and hot pressed at 973K, four of which (with relatively higher doping levels) are shown here in Figure S2. Except the samples with highest doping levels ($x = 0.25$ and $x = 0.30$ with less than 1% Yb-rich impurities), all of the other samples show a single-phase skutterudite microstructure (the contrast in SEM images is from different grain orientation). These results are consistent with our XRD data shown in Figure S1.

Electron probe microanalysis (EPMA) measurements were carried out at ten different locations on the skutterudite phase region and the average Yb contents are listed in Table S1. EPMA results of samples with Yb nominal content less than $x = 0.025$ are not listed due to precision limitation. The sample with a

DOI: 10.1038/NMAT4430

Yb nominal content of x = 0.20 is characterized by Energy Dispersive Spectroscopy (EDS) rather than EPMA. Except the sample with x = 0.30, all the other samples have an actual Yb content that is very close to nominal content. This is in agreement with SEM results, which show that the x = 0.30 sample has the highest amount of Yb-rich impurities (less than 1 volumic percent).

Table S1. Actual Yb content in the skutterudite phase estimated by EPMA or EDS for Yb-containing skutterudites with different nominal compositions.

Samples	Nominal Yb content	EPMA Yb content
$Yb_{0.025}Co_4Sb_{12.012}$	0.025	0.019 ± 0.009
$Yb_{0.05}Co_4Sb_{12.012}$	0.05	0.047± 0.009
$Yb_{0.075}Co_4Sb_{12.012}$	0.075	0.071 ± 0.009
$Yb_{0.1}Co_4Sb_{12.012}$	0.1	0.101 ± 0.013
$Yb_{0.2}Co_4Sb_{12.012}$	0.2	0.19 ± 0.02 (EDS)
$Yb_{0.25}Co_4Sb_{12.012}$	0.25	0.249 ± 0.013
$Yb_{0.3}Co_4Sb_{12.012}$	0.3	0.259 ± 0.013

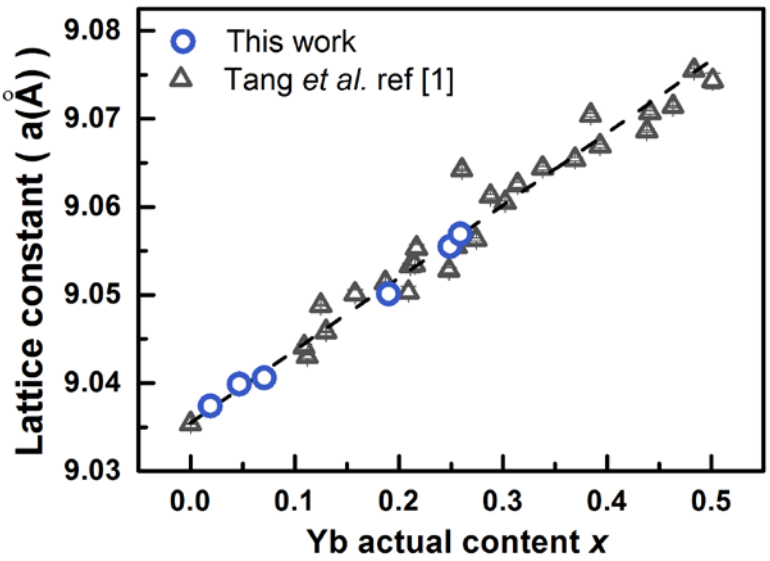

Figure S3. Dependence of lattice parameter on the actual Yb content, x, in $Yb_xCo_4Sb_{12}$ for samples in this study and samples in ref 1 [1].

Lattice parameters were derived from powder X-ray diffraction data and plotted against Yb actual content determined from EPMA, as shown in Figure S3. We can see that there is a good linear relationship between the actual Yb content and lattice parameter of the skutterudite phase, which agrees with the literature data[1] and is consistent with Yb going into the same site across the whole range (up to x=0.26), presumably the void site.

Transport Property Measurement

The transport properties of $Yb_xCo_4Sb_{12}$ skutterudites (with nominal x from 0.005 to 0.3) were measured up to 850K, and the results are shown in Figure S4. The maximum zT reaches 1.3 for both x = 0.25 and x = 0.30 samples at 850K. Room temperature transport properties are shown in Table S2.

Table S2. Room temperature transport properties of $Yb_xCo_4Sb_{12}$ skutterudites (with nominal x from 0.0025 to 0.3).

Nominal x	n_H (cm^{-3})	Seebeck (μVK^{-1})	Mobility ($cm^2V^{-1}s^{-1}$)	Resistivity ($10^{-5}\Omega m$)	κ ($Wm^{-1}K^{-1}$)
0.0025	6.8E+17	-369.2	150.3	61.16	-
0.005	3.5E+18	-320.8	79.4	22.27	8.68
0.0075	5.7E+18	-306.4	82.4	13.34	6.85
0.01	7.4E+18	-298.8	80.1	10.54	6.93
0.025	2.1E+19	-241.8	98.1	3.08	5.59
0.05	4.6E+19	-196.8	86.0	1.57	4.81

DOI: 10.1038/NMAT4430

0.075	7.37E+19	-172.8	78.5	1.08	3.86
0.1	1.24E+20	-152.4	69.4	0.73	4.02
0.2	2.87E+20	-120.6	36.4	0.60	2.99
0.25	4.26E+20	-102.2	39.5	0.37	3.63
0.3	5.08E+20	-95.0	35.9	0.34	3.64

(a)

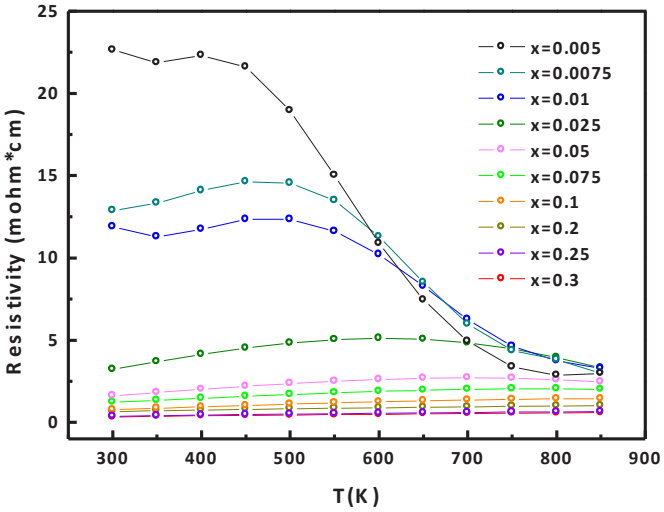

(b)

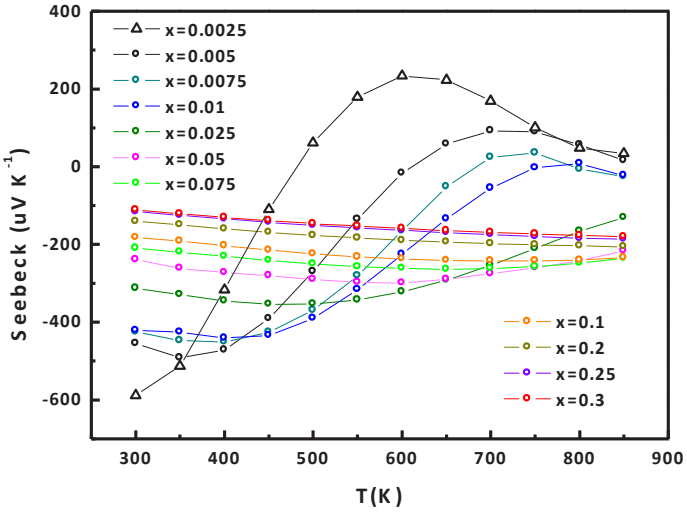

DOI: 10.1038/NMAT4430

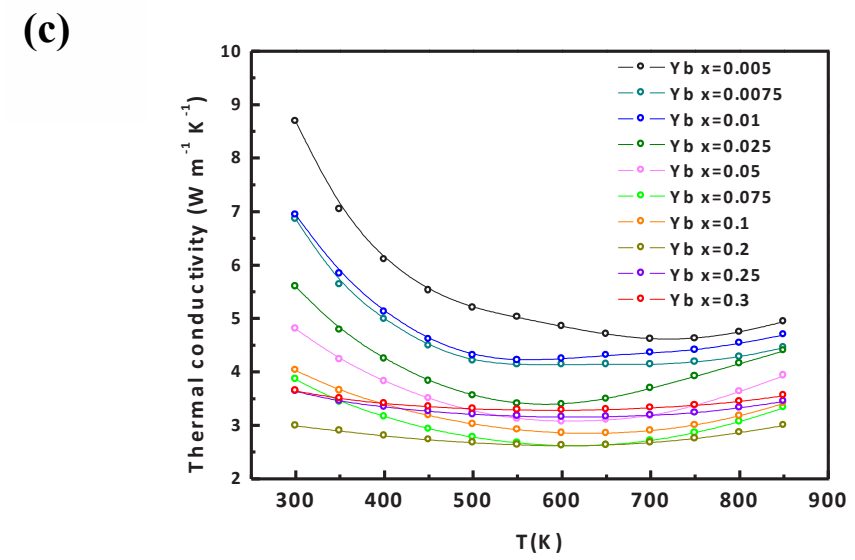

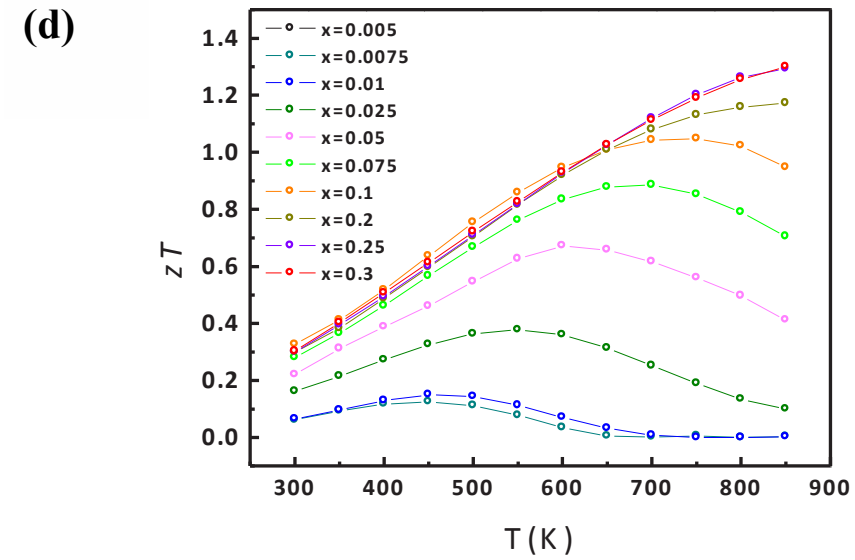

Figure S4: Temperature dependent transport properties of $Yb_xCo_4Sb_{12.012}$ skutterudites (x from 0.005 to 0.3): (a) Resistivity; (b) Seebeck coefficient; (c) Thermal conductivity; (d) *zT*.

Optical Measurements

In skutterudite systems other than $CoSb_3$, the literature has been sparse regarding optical data. Slack did publish a result for $IrSb_3$ which suggested a large optical gap (more than 1 eV) [2]. One recent thesis report by Ni shows that photo-acoustic measurements on undoped $CoSb_3$ compounds show an absorption edge around 0.3 eV [3] (although they do not observe the first transition). Optical measurements have also been performed over a wide range of frequencies by Matsunami *et al*. on Ce-filled skutterudites (with Fe, Ru, and Os); these show band gaps within 0.2-0.3 eV, although additional analysis regarding other interband transition near the fundamental absorption edge is not discussed [4].

Other possibilities exist for the two distinct absorption edges that should be considered. First, a shallow absorption feature before the primary gap can be observed either in the case of intrinsic disorder/alloying in the sample (Urbach edge) or by intrinsic defect states which lay in the gap. However, because optical measurements were performed on the undoped sample that showed nearly intrinsic behavior, we do not expect the effects due to alloying or disorder. The possibility of a deep, intrinsic defect state lying within the band gap is possible; to exclude this as a possibility a series of lightly doped samples was also measured. We measured both extrinsically doped (filled with Yb or Na) and intrinsically doped (Co rich, Sb rich, Co poor, Sb poor) to encourage any intrinsic or extrinsic defect states to grow in number. Absorption edge measurements indicated no appreciable change in the strength of transition 1 relative to transition 2 that was not consistent with the addition of free carriers into the sample alone; therefore, we conclude that transition 1 is not a result of defect states.

While Transition 1 has been shown to be approximately constant with respect to temperature (Figure 3b), a slight decrease is observed ($\frac{dE_{g,\Gamma-\Gamma}}{dT} \approx 6\times10^{-5}\ eV/K$). Regardless, effective convergence ($\Delta E < 1k_BT$) occurs for temperatures greater than 500 K.

DOI: 10.1038/NMAT4430

Multi-band Transport Model

In this work, a three band transport model was used to calculate the thermoelectric properties for $CoSb_3$ at T=300 and 800 K. The properties were calculated assuming acoustic phonon scattering[5] for all bands by solving the chemical potential dependent Boltzmann transport equations detailed in the appendix of Ravich *et al.* [5] for non-parabolic bands (parabolic bands were modeled assuming $\beta = 0$). The appropriate transport integrals were computed numerically (in Python using customized functions that used the numpy and scipy computational packages) to determine the η-dependent Seebeck, mobility, carrier concentration, etc. for each band[6]. The overall properties were computed using conductivity weighted averages as described by Putley[7] for a system of two conduction bands (CB_Γ and CB_2) and one valence band.

We determine the room temperature density of states effective masses of CB_Γ and CB_2 to be 0.7 and 4.8 m_e with deformation potentials of 37.2 and 20.4 eV respectively and a band offset of 0.08 eV. The valley degeneracies for these bands were assumed to be 3 and 12 respectively (as suggested from the DFT calculations). The anisotropy factor was assumed to be 5.0 for CB_Γ to reflect the three widely varying effective masses of the converged bands at the conduction band minimum. Including the valence band in the calculations was necessary (particularly at high temperatures); the best fit of its parameters were found to be: $N_v = 1$ (valence band maximum exists at Γ), $m_d^* = 0.6\, m_e$, $\beta = 0$ (parabolic), and $E_{def} = 7.8$ eV with a band gap of 0.22 eV.

At high temperatures (800K), the conduction band offset was taken to be: $\Delta E = 0.0$ eV in accordance with the optical observation of band convergence. The density of states effective masses were fit to be 0.42 and 2.88 m_e with deformation potentials of 44.5 and 24.4 eV for the CB_Γ and CB_2 respectively. The valley degeneracy and anisotropy parameters were assumed to be the same as at 300 K. The valence band parameters were adjusted at these high temperatures to accommodate for the much larger bipolar effect; the effective mass was taken to be 0.6 m_e with a deformation potential of 20 eV and

a band gap of 0.22 eV (which is shown to be approximately constant from optical measurements). Because of the large bipolar effects, high temperature Hall-effect measurements (and carrier concentrations) are not reliable; room temperature n_H was plotted instead (even for high temperature properties). In order to compute the room temperature Hall carrier concentration for the three band model, the charge neutrality equation: $N_A - N_D = \sum_i p_i(\eta, T) - \sum_i n_i(\eta, T)$, was solved at high temperature to determine the intrinsic defect concentration (N_A-N_D as a function of η at 800 K) which was then projected back to room temperature (solved for an equivalent η_{300K}) from which the room temperature Hall coefficient (R_H) and n_H could be calculated. zT is computed for each band model assuming a polynomial fit to the experimental values for the total thermal conductivity (Figure 3c). The representative zT for each band is computed by performing a two band calculation using either CB_Γ and VB or CB_2 and VB for the primary and secondary conduction band zT, respectively.

We should note that while these values yielded acceptable fits of the properties at these particular temperatures, the fits are not unique. In other words, other sets of parameters may provide adequate fits. The fit provides a quantitative example that a multi-band description can adequately reflect the nature of both transport and optical measurements.

Kane Band Mott Relation

In this work, we have shown that the non-parabolic Kane band relation yields a decreasing Seebeck-dependent effective mass as carrier concentration increases. This is significant because it not only shows that the common explanation of Kane bands causing the increasing mass with doping in $CoSb_3$ is inadequate, but also this should have wider implications in terms of non-parabolicity's contribution to thermoelectric performance. The well-known Mott relation is [8]:

$$S = \frac{\pi^2 k_B^2 T}{3e} \frac{1}{\sigma_E} \frac{d\sigma_E}{dE} \qquad \text{Eq. S1}$$

DOI: 10.1038/NMAT4430

where $\sigma_E = \frac{e^2}{3} v(E)^2 \tau(E) D(E)$ is the energy dependent electronic conductivity[9] that depends on the electron drift velocity (v), the scattering time (τ), and the density of states (D). Using the relationships given previously by Young *et al.*[10] we can show that $v(E) = \frac{1}{\hbar}\frac{dE}{dk} = \sqrt{\frac{2}{m_0^*}}\left(\frac{d\gamma}{dE}\right)^{-1}\gamma^{1/2}$, $D(E) = \frac{\sqrt{2}m_0^{*3/2}}{\pi^2\hbar^3}\gamma^{1/2}\frac{d\gamma}{dE}$, and $\tau = \tau_0\gamma^{r-\frac{1}{2}}\left(\frac{d\gamma}{dE}\right)^{-1}$ where $\gamma(E) = \frac{\hbar^2 k^2}{2m_0^*}$. The Mott relation for a general band becomes:

$$S = \frac{2}{3}\frac{k_B^2 T}{e\hbar^2}\left(\frac{\pi}{3n}\right)^{2/3} m_0^* \frac{d\gamma}{dE}[r + 1 - \lambda] \qquad \text{Eq. S2}$$

$$\text{where } \lambda = 2\gamma\left(\frac{d\gamma}{dE}\right)^{-2}\frac{d^2\gamma}{dE^2} \qquad \text{Eq. S3}$$

This expression (Eq.S2) is derived by differentiating the obtained expression for $\sigma_E = \frac{2^{3/2}m_0^{*1/2}e^2\tau_0}{3\pi^2\hbar^3}\left(\frac{d\gamma}{dE}\right)^{-2}\gamma^{r+1}$.

$$\frac{d\sigma_E}{dE} = \frac{2^{3/2}m_0^{*1/2}e^2\tau_0}{3\pi^2\hbar^3}\left(\left(\frac{d\gamma}{dE}\right)^{-1}(r+1)\gamma^r - 2\left(\frac{d\gamma}{dE}\right)^{-3}\frac{d^2\gamma}{dE^2}\gamma^{r+1}\right) \qquad \text{Eq. S4}$$

which upon substitution into the Mott equation (Eq. S1) yields the energy dependent Seebeck relation:

$$S = \frac{\pi^2 k_B^2 T}{3e\gamma}\frac{d\gamma}{dE}\left(r + 1 - 2\gamma\left(\frac{d\gamma}{dE}\right)^{-2}\frac{d^2\gamma}{dE^2}\right) \qquad \text{Eq. S5}$$

Next, we must first approximate the carrier concentration as a function of Fermi level: $n \approx \int_0^{E_F} D(E)dE = \frac{2^{3/2}m_0^{*3/2}}{3\pi^2\hbar^3}\gamma^{3/2}\Big|_{E=E_F}$, which can be solved for $\gamma(n) = \frac{\hbar^2}{2m_0^*}(3\pi^2 n)^{2/3}$ and substituted into Eq. S5 to obtain the final expression (Eq. S2). In order to obtain the m_S^* that is presented in the main text for Kane band, we substitute $\gamma = E + E^2/E_g$ as is commonly used by Ravich *et al.* [5], $\frac{d\gamma}{dE} = 1 + 2E/E_g$, and $\frac{d^2\gamma}{dE^2} = 2/E_g$ into Eq. S2. Upon substituting in λ (Eq. S3) and simplifying, we obtain

$m_S^*(E) = \frac{m_0^*}{1+2E/E_g}$ by inspection. It should be noted that this result only holds for r=0 (acoustic phonon scattering). Alternative scattering mechanisms can show increases in the energy dependent m_S^* [11].

While the derivation from the main text assumes a simpler scattering time where the matrix element coupling valence and conduction band state is independent of electron energy, Ravich *et al.* suggested an alternative form for the acoustic phonon scattering time that includes an energy dependent matrix element [5,12]. Upon simplification, the expression for the scattering time can be shown to be:

$$\tau(E) = \frac{3\hbar\, C_l N_v}{\pi k_B T D(E) E_{def}^2}\left(1+\frac{2E}{E_g}\right)^2\left(\left(1+\frac{2E}{E_g}\right)^2+2\right)^{-1} \quad \text{Eq. S6}$$

Where $C_l = \rho v_l^2$ (v_l is the longitudinal speed of sound) and E_{def} is the acoustic phonon deformation potential. In this case, the equivalent Mott relation can be derived (using Eq. S1 with the modified σ_E); we find the Seebeck effective mass simplifies to:

$$m_S^*(E) = \frac{3m_0^*\left(1+\frac{2E}{E_g}\right)}{\left(1+\frac{2E}{E_g}\right)^2+2} \quad \text{Eq. S7}$$

Which also tends to decrease with energy at high Fermi levels, but initially shows a small increase (of only a few percent).

DFT Computed Fermi Surfaces

In general, the determination of the band gap of skutterudites is a challenging task. For instance, the experimental values for $CoSb_3$ vary over a wide range of energy: 0.031[13], 0.035[14], 0.05[15], 0.55[16], 0.63[17] eV depending on the method by which the estimate is obtained.

Analogously, the reported theoretical band gaps also fluctuate over a similar wide range and are highly sensitive to the simulation parameters. Nonetheless, while Perdew-Burke-Ernzerhof (PBE)[18] density functional is generally known for the systematic underestimation of the band gap of

DOI: 10.1038/NMAT4430

semiconductors, it can usually predict the correct topology of the bands; for such cases, the PBE electronic structure can simply be corrected by an energy shift of the unoccupied manifold via the scissor operator[19].

In that regard, the PBE functional has been shown to be satisfactory for calculating the electronic states of $CoSb_3$. Koga *et al.*[20] found that the PBE (occupied and unoccupied) bands yield theoretical optical spectra that agree well with experimental near edge x-ray absorption and emission spectra (XANES/XENES). The PBE valence bands also reproduce well the experimental ultraviolet photoemission spectroscopy (UPS)[14] data.

Furthermore, the more rigorous quasiparticle GW method, known to systematically reproduce experimental band gaps, yields a value of 0.335 eV [21], close to our PBE result of 0.23 eV.

The DFT calculated Fermi Surfaces at various energy levels are shown in Figure S5.

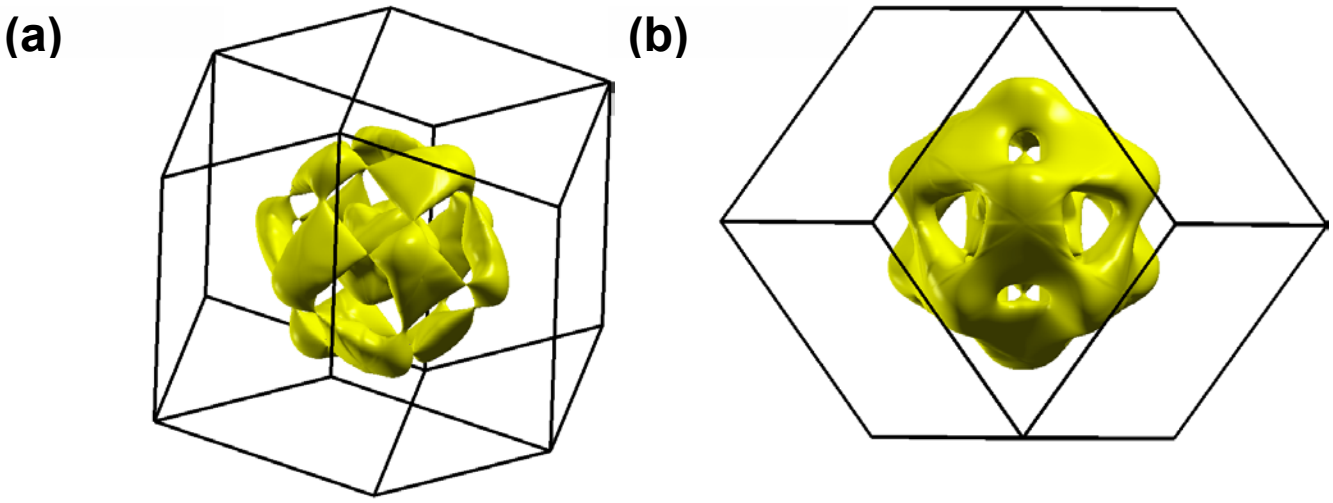

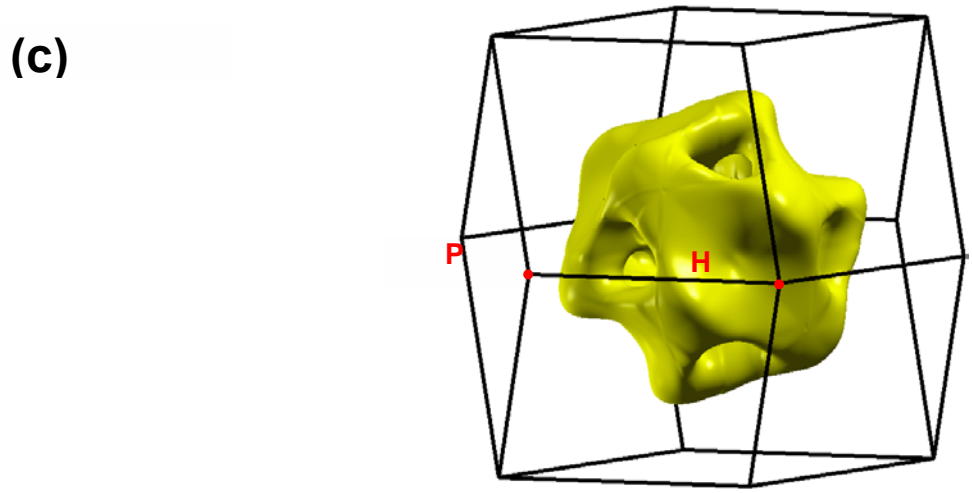

Figure S5: a) Fermi surface for Fermi levels 0.13eV above the conduction band edge showing the 12 pockets of the second conduction band CB_2 joining near $\Gamma - F$. b) Fermi surface at 0.14eV above the conduction band edge showing the connection of the CB_2 surface to the Γ surface near the $\Gamma - N$ line. The joining is observable in b) through the small hole along $\Gamma - H$ that closes in c) at 0.147 eV.

Supplementary References

1 Tang, Y., Chen, S.-w. & Snyder, G. J. Temperature dependent solubility of Yb in Yb–CoSb3 skutterudite and its effect on preparation, optimization and lifetime of thermoelectrics. *Journal of Materiomics* **1**, 75-84, doi:10.1016/j.jmat.2015.03.008 (2015).

2 Slack, G. A. & Tsoukala, V. G. Some Properties of Semiconducting Irsb3. *J Appl Phys* **76**, 1665-1671, doi:Doi 10.1063/1.357750 (1994).

3 Ni, G. *Photoacoustic measurements of bandgaps of thermoelectric materials* Master of Science thesis, Massachusetts Institute of Technology, (2014).

4 Matsunami, M. *et al.* Optical Conductivity and Electronic Structures in Ce-Filled Skutterudites. *J Phys Soc Jpn* **77**, 315-317, doi:10.1143/JPSJS.77SA.315 (2008).

5 Ravich, Y. I., Efimova, B. A. & Smirnov, I. A. *Semiconducting Lead Chalcogenides* Vol. 5 (Plenum Press, 1970).

6 May, A. F. & Snyder, G. J. in *CRC Handbook of Thermoelectrics* (ed D. M. Rowe) (CRC Press, 2011).

7 Putley, E. H. Galvano- and thermo-magnetic coefficients for a multi-band conductor. *Journal of Physics C: Solid State Physics* **8**, 1837 (1975).

8 Heremans, J. P. *et al.* Enhancement of thermoelectric efficiency in PbTe by distortion of the electronic density of states. *Science* **321**, 554-557, doi:DOI 10.1126/science.1159725 (2008).

9 Mizutani, U. *Introduction to the electron theory of metals*. (Cambridge University Press, 2001).

10 Young, D. L., Coutts, T. J., Kaydanov, V. I., Gilmore, A. S. & Mulligan, W. P. Direct measurement of density-of-states effective mass and scattering parameter in transparent conducting oxides using second-order transport phenomena. *Journal of Vacuum Science & Technology A* **18**, 2978-2985, doi:doi:http://dx.doi.org/10.1116/1.1290372 (2000).

11 Gibbs, Z. M. *Band Engineering in Thermoelectric Materials Using Optical, Electronic, and Ab-initio Computed Properties* PhD thesis, California Institute of Technology, (2015).

12 Wang, H., Pei, Y., LaLonde, A. D. & Snyder, G. J. Weak electron–phonon coupling contributing to high thermoelectric performance in n-type PbSe. *Proceedings of the National Academy of Sciences* **109**, 9705-9709, doi:10.1073/pnas.1111419109 (2012).

13 Arushanov, E., Respaud, M., Rakoto, H., Broto, J. M. & Caillat, T. Shubnikov–de Haas oscillations in CoSb3 single crystals. *PHYSICAL REVIEW B* **61**, 4672 (2000).

14 Ishii, H. *et al.* Photoemission study of the skutterudite compounds CoSb3 and RhSb3. *Journal of the Physical Society of Japan* **71**, 2271-2275, doi:10.1143/JPSJ.71.2271 (2002).

15 Mandrus, D. *et al.* Electronic transport in lightly doped $CoSb_3$. *Physical Review B* **52**, 4926-4931 (1995).

16 Nolas, G. S., Slack, G. A., Caillat, T. & Meisner, G. P. Raman scattering study of antimony - based skutterudites. *Journal of Applied Physics* **79**, 2622-2626, doi:doi:http://dx.doi.org/10.1063/1.361132 (1996).

17 Fleurial, J. P., Caillat, T. & Borshchevsky, A. in *Thermoelectrics, 1997. Proceedings ICT '97. XVI International Conference on.* 1-11.

18 Perdew, J. P., Burke, K. & Ernzerhof, M. Generalized Gradient Approximation Made Simple. *Phys Rev Lett* **77**, 3865-3868 (1996).

19 Levine, Z. H. & Allan, D. C. Linear optical response in silicon and germanium including self-energy effects. *Physical Review Letters* **63**, 1719-1722, doi:10.1103/PhysRevLett.63.1719 (1989).

20 Koga, K., Akai, K., Oshiro, K. & Matsuura, M. Electronic structure and optical properties of binary skutterudite antimonides. *Physical Review B* **71**, 155119 (2005).

21 Khan, B. *et al.* Electronic band structures of binary skutterudites. *Journal of Alloys and Compounds* **647**, 364-369, doi:http://dx.doi.org/10.1016/j.jallcom.2015.06.018 (2015).